

## Norwegian Remote Sensing Experiment in a Marginal Ice Zone

NORSEX Group

The Norwegian Remote Sensing Experiment (NORSEX) consisted of three field investigations in Norwegian waters. The first investigation was of the sea surface temperature and wind in the Norwegian and Barents seas in November 1978, as derived from the scanning multichannel microwave radiometer (SMMR) on the Nimbus 7 satellite (1). In the second investigation, conducted off the west coast of Norway in spring 1979, remote sensing methods were used to obtain a better understanding of the dynamics of the Norwegian Coastal Current (2).

The third investigation took place in the marginal ice zone north of Svalbard from 17 September 1979 to 12 October 1979 and is the subject of this article. The objective was to obtain a better understanding of the interactive processes among air, ice, and water in the marginal ice zone. To accomplish this objective, active and passive microwave remote sensing systems were used to study the location and structure of the ice edge, eddies in the edge region, wave propagation into the ice pack, distribution of ice

The NORSEX Group consists of the following individuals: B. Farrelly, J. A. Johannessen, O. M. Johannessen, and E. Svendsen (Geophysical Institute, Division A, University of Bergen, Bergen, Norway); K. Kloster (Christian Michelsen Institute, Bergen); I. Horjen (Norwegian Hydrodynamic Laboratories, Trondheim); C. Mätzler (Institute of Applied Physics, University of Bern, 3012 Bern, Switzerland); W. J. Campbell (U.S. Geological Survey, Tacoma, Washington 98416); J. Crawford, R. Harrington, L. Jones, C. Swift, and V. E. Delnore (NASA/Langley Research Center, Hampton, Virginia 23365); D. Cavaliere and P. Gloersen (NASA/Goddard Space Flight Center, Greenbelt, Maryland 20771); S. V. Hsiao, O. H. Shemdin, and T. W. Thompson (Jet Propulsion Laboratory, Pasadena, California 91103); and R. O. Ramseier (Atmospheric Environmental Services, Ottawa, Ontario, Canada K1A 0H3). O. M. Johannessen and W. J. Campbell are the coordinators.

types, and ice concentration. Surface and airborne microwave observations at many frequencies, together with in situ measurements, validated and refined the Nimbus 7 SMMR ice-ocean algorithms. The in situ measurements were obtained with an oceanographic and ice physics program that included drift buoys in the ice pack and ocean and standard meteo-

**Summary.** The Norwegian Remote Sensing Experiment in the marginal ice zone north of Svalbard took place in fall 1979. Coordinated passive and active microwave measurements were obtained from shipborne, airborne, and satellite instruments together with in situ observations. The obtained spectra of emissivity (frequency range, 5 to 100 gigahertz) should improve identification of ice types and estimates of ice concentration. Mesoscale features along the ice edge were revealed by a 1.215-gigahertz synthetic aperture radar. Ice edge location by the Nimbus 7 scanning multichannel microwave radiometer was shown to be accurate to within 10 kilometers.

rological observations. This article discusses some of the remote sensing observations from aircraft and surface-based sensors and evaluates the accuracy of the Nimbus 7 SMMR in detecting the position of the ice edge. The NORSEX sea ice algorithm for the Nimbus 7 SMMR and the air-ice-ocean interaction in the marginal ice zone are addressed elsewhere (3, 4).

### Description of Experiment

During the experiment a variety of ice types were present, including first-year ice ("pancakes"), second and multiyear ice, and some new ice forms (5). Ice drift averaged about 10 cm/sec in a southwest direction, in accordance with earlier ob-

servations (6). However, there were variations of 20 cm/sec over a few days. A water mass of low salinity (32.5 per mil) and low temperature ( $-1.75^{\circ}\text{C}$ ) extended 20 m below the ice pack. Off the ice edge, this water mass encountered another water mass with a higher salinity (33.4 per mil) and temperature ( $-0.5^{\circ}\text{C}$ ), causing an ocean front. Below these two surface water masses the Atlantic core of warm ( $1.50^{\circ}\text{C}$ ) and high-salinity (34.9 per mil) water was located at 250 m.

The Nimbus 7 SMMR imaged the test region three times every other day. The SMMR operates at five different frequencies, 6.6, 10.7, 18.0, 21.0, and 37.0 GHz, with horizontal and vertical polarization and with spatial resolution cells of 148 by 95, 91 by 59, 55 by 41, 46 by 30, and 27 by 18 km, respectively. The instrument has a conical scan with an incidence angle of  $50^{\circ}$  (7). No useful data on the ice were retrieved from visible

light and infrared sensors in the TIROS and NOAA satellites because of cloud cover, which during this season frequently obscures the marginal ice zone.

Two remote sensing aircraft from NASA (a C-130 and a CV-990) took part in the experiment. The sensors on the C-130 aircraft included a 14.6-GHz airborne microwave scatterometer (AMSCAT), a 13.3-GHz scatterometer, a 4.5- to 7.2-GHz stepped frequency microwave radiometer (SFMR), an 18.0-, 21.0-, and 37.0-GHz multifrequency microwave radiometer (MFMR), a 10.7-GHz passive microwave imaging system (PMIS), a thermal infrared radiometer (PRT-5), and two Zeiss metric cameras. Six flights were conducted over the marginal ice zone.

The NASA CV-990 was instrumented

with a Jet Propulsion Laboratory L-band (1.215-GHz) synthetic aperture radar (SAR) with a resolution of 25 m (8). Two flights were performed, one of which was simultaneous with a C-130 flight.

A combined passive and active microwave sensor system measured ice and ocean signatures at a height of 6.5 m from the R.V. *Polarsirkel*, an icebreaker. These sensors, from the University of Bern, included five microwave radiometers at 4.9, 10.4, 21, 36, and 94 GHz, a scatterometer at 10.4 GHz, and an infrared PRT-5 (9–11).

The major platform for the surface and subsurface observations in situ was the *Polarsirkel*, which operated in the test area from 17 September to 3 October.

To interpret the radiometric measurements, cores from multiyear ice were obtained that gave vertical profiles of temperature, salinity, and density. Samples of pancake ice were also obtained, but these were of limited use because of brine drainage. Photographs were taken of every radiometric target.

The oceanographic program included conductivity, temperature, and depth (CTD) stations (12) in sections perpendicular to and along the ice edge, towed surface temperature sensors, and salinity sampling with buckets. Deployment of four ocean surface drifters and four ice floe drifters equipped with ARGOS tracking systems was done from the *Polarsirkel*. One of the buoys on the ice had an

array of six Aanderaa current meters, with the deepest at 300 m. Four drift buoys with atmospheric pressure sensors, air and ice temperature sensors, and ARGOS data transmission and positioning systems were parachuted onto the ice by a Norwegian Air Force P3 in an array covering 200 by 200 km, with the center of the array 150 km from the ice edge. Standard meteorological observations were carried out from the *Polarsirkel*. Figure 1 shows the locations of the CTD stations, the drift buoys, and the ice edge on 26–27 September.

During the experiment the positions of the drift buoys were sent regularly from Tromsø telemetry station to the *Polarsirkel*, where preliminary analysis of the data was carried out. This provided near-real-time control of the progress of the experiment—a necessity for proper planning of the remote sensing flights in the ice edge region.

#### Surface-Based Microwave Observations

The microwave instruments on the *Polarsirkel* were mounted for rotation about appropriate axes to collect data as a function of nadir angle and polarization. Figure 2 shows typical ice conditions in the ice edge region, from newly frozen, thin pancakes to snow-covered, multiyear floes. The vertical structure of a multiyear floe showed two to three

horizontal layers of thin ice to be present in the snow cover, which was 10 to 15 cm thick. In the snow-ice interface very large snow crystals were observed, and the transition from snow to ice was diffuse. The vertical salinity profile of the floe was nearly constant at about 0.5 per mil.

From the beginning of the microwave observations on 21 September to the end of 2 October the snow cover remained dry. Wet snow would have masked the ice signatures. The temperature of the snow surface closely followed the air temperature, whereas a few centimeters below the snow-ice interface the temperature was constant between  $-0.5^{\circ}$  and  $-1.0^{\circ}\text{C}$ . This indicates that infrared temperature measurements of the snow surface are not usable for deducing microwave emissivity, since microwaves are mainly emitted from the upper part of the ice and not from the snow surface. For this reason an ice temperature of  $-1.0^{\circ}\text{C}$  was used in the calculations of emissivity.

Surface-based measurements of physical temperature and of surface and sky brightness temperatures have the potential to separate effects of the targets from those of the atmosphere. Knowledge of the total scattering coefficient  $\gamma$  (13) enables us to separate the observed targets into quasi-specularly reflecting surfaces (open water, grease ice) and diffuse scatterers of the Lambert type (rough pan-

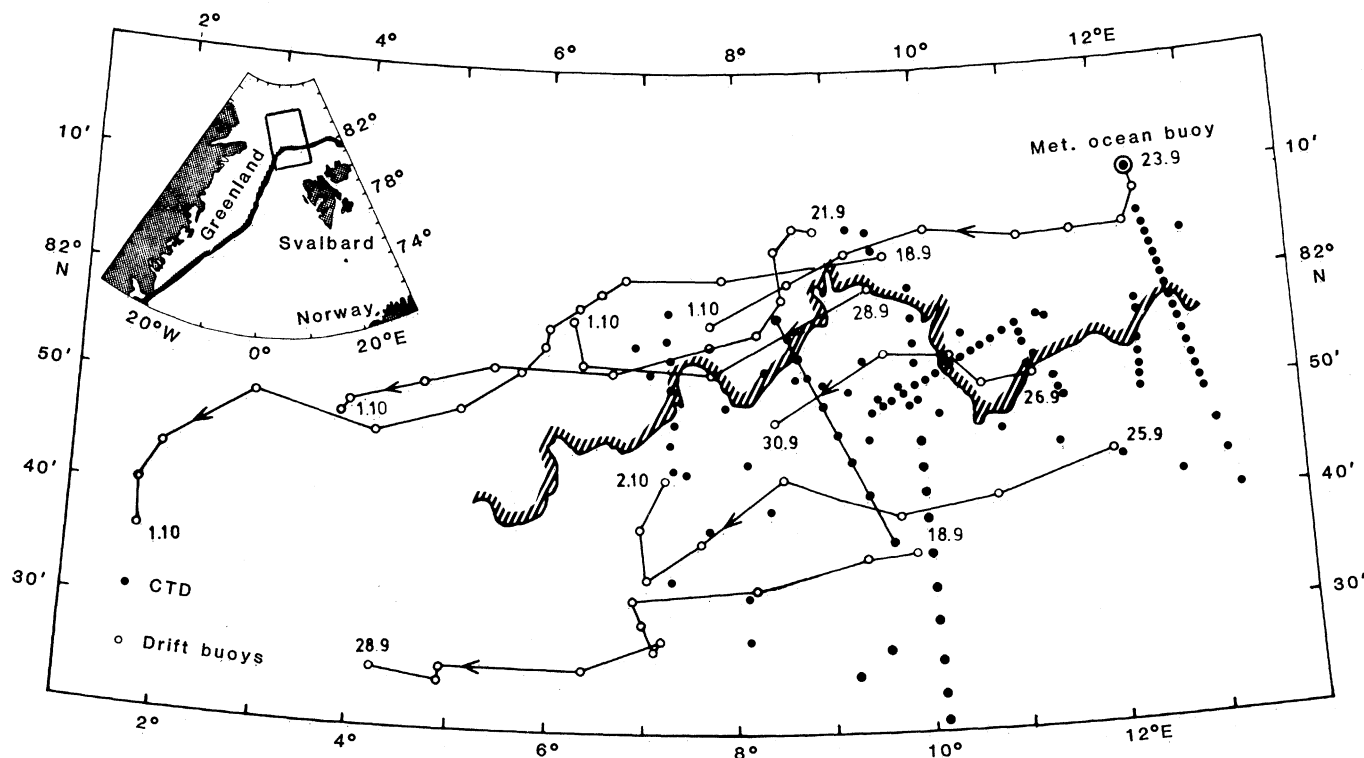


Fig. 1. Schematic representation of the ice edge located by the R.V. *Polarsirkel* on 26–27 September, the CTD stations, and the drift buoys in the experimental area. Inset: map showing the location of the experimental area (box).

cakes, second and multiyear ice). The resulting parameters are emissivity and opacity, which are important for validation and refinement of the Nimbus 7 SMMR ice-ocean algorithms.

The measured brightness temperature  $T_b(\theta)$  is the sum of the brightness temperature emitted from the target and reflected sky radiation:

$$T_b(\theta) = e(\theta)T + [1 - e(\theta)]T_{\text{sky}}(\theta_{\text{eff}})$$

where  $e(\theta)$  is emissivity as a function of nadir angle  $\theta$ ,  $T$  is physical temperature of the emitting medium, and  $T_{\text{sky}}(\theta_{\text{eff}})$  is incoming sky brightness temperature from effective angles of  $180^\circ - \theta$  for a specular reflector and  $120^\circ$  for a Lambert scatterer.

Measurements of the brightness temperature of calm water (winds less than 3 m/sec) were conducted at water temperatures close to the freezing point. The corresponding emissivities,  $e_h$  for horizontal polarization and  $e_v$  for vertical polarization at a nadir angle of  $50^\circ$ , are shown in Table 1 together with the theoretical values. These values were generated from the Fresnel formulas by using the dielectric properties given by Stogren (14). The theoretical emissivities should be correct to within 0.02, which is also the approximate error associated with a  $3^\circ$  uncertainty in viewing angle due to heeling of the ship. This effect explains most of the variation in the measured emissivities of calm water. Except for the values at 21 and 94 GHz there is very good agreement between the theoretical and measured emissivities.

The measured emissivities of calm water, snow-covered multiyear ice, and first-year (pancake) ice are compared in Fig. 3. The first-year signature corresponds to ice that is thicker than 3 cm. (The emissivity of thinner pancakes varied strongly with thickness.) Open water exhibits a large difference between the polarization components and in increasing emissivity with increasing frequency. The signature of first-year ice is almost independent of polarization, with an emissivity close to unity and independent of frequency. The emissivity of multiyear ice decreases with increasing frequency and shows some polarization throughout the measurement band. Figure 3 shows that low frequencies can be used for deducing total ice concentration because of the large difference in emissivity between water and both ice types. Furthermore, a large difference in emissivity between multiyear and first-year ice is seen at high frequencies, making it possible to separate the amount of each of these different ice types. There is an

indication that ice concentration can also be retrieved from the highest frequency because of the polarization difference between water and ice. This would result in better spatial resolution from satellites.

The mean emissivities shown in Fig. 3 are also given in Table 1, together with the total variability of the various measurements. Interference effects from multiple reflections in the strongly layered snow cover are responsible for part

of the variability. Since these effects play a disturbing role only in surface-based measurements with a small footprint, the systematic variability associated with remote sensing is smaller than indicated in Table 1. The variability in the measurements of pancake ice is probably a direct result of the surface wetness of the new ice, which indirectly is a function of ice thickness.

Measured and theoretical (15) atmospheric opacities ( $\tau_0$ ) are also given in

Table 1. Near-surface measurements of the emissivity ( $\theta = 50^\circ$ ), with maximum variability, of calm water, first-year ice (F.Y.) and multiyear ice (M.Y.). Theoretical calculations of the emissivity of calm water are shown for comparison. Zenith atmospheric opacities—theoretical values and mean values  $\pm$  standard deviations measured during the 13-day period of ship-based measurements—are also given. All values have been multiplied by  $10^3$ .

Variable	Frequency (GHz)				
	4.9	10.4	21	36	94
$e_v$ (theory)	505	541	613	692	846
$e_v$ (water)	505 $\pm$ 9	545 $\pm$ 10	633 $\pm$ 15	685 $\pm$ 14	753 $\pm$ 26
$e_h$ (theory)	252	275	324	386	538
$e_h$ (water)	256 $\pm$ 9	281 $\pm$ 10	354 $\pm$ 10	387 $\pm$ 12	488 $\pm$ 50
$e_v$ (F.Y.)	931 $\pm$ 10	939 $\pm$ 14	953 $\pm$ 3	945 $\pm$ 1	934 $\pm$ 15
$e_h$ (F.Y.)	845 $\pm$ 65	880 $\pm$ 46	906 $\pm$ 25	904 $\pm$ 21	895 $\pm$ 9
$e_v$ (M.Y.)	926 $\pm$ 37	886 $\pm$ 59	787 $\pm$ 80	675 $\pm$ 75	566 $\pm$ 50
$e_h$ (M.Y.)	865 $\pm$ 49	712 $\pm$ 58	635 $\pm$ 125	582 $\pm$ 68	535 $\pm$ 61
$\tau_0$ (theory)	10	13	43	56	150
$\langle \tau_0 \rangle^*$ (measurement)	11 $\pm$ 8	15 $\pm$ 9	62 $\pm$ 16	73 $\pm$ 16	140 $\pm$ 35

\*Brackets indicate average.

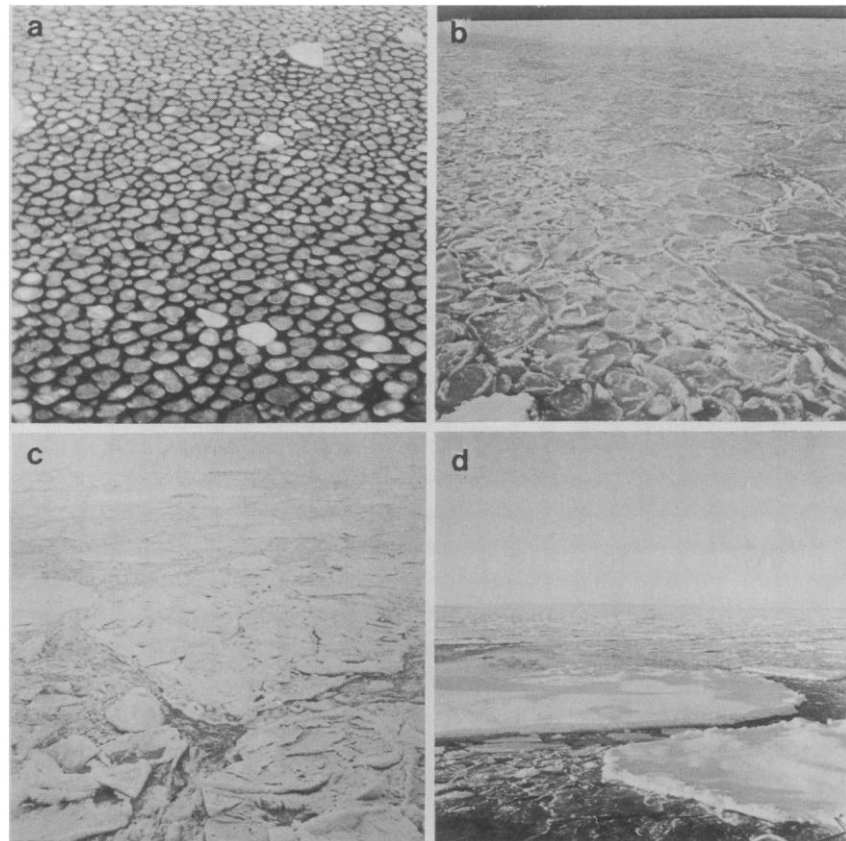


Fig. 2. Typical ice types in the ice edge region. (a) Very thin pancakes, 15 to 20 cm in diameter. (b) Densely packed pancakes, 3 cm thick and 0.5 m in diameter. (c) Pancakes 20 cm thick and 1 to 2 m in diameter. (d) Multiyear ice with floes 3 to 4 m thick and 20 m in diameter.

Table 1. Oxygen and water vapor absorption were taken into account; liquid water was neglected. There is no significant difference between the measured and theoretical opacities. The tendency for the measured opacities to be somewhat higher than the theoretical opacities may be due to liquid water absorption caused by the frequent presence of low clouds. There was a weak tendency toward increasing opacity with increasing air temperature. However, the small range in air temperature does not allow correlation analysis.

Figure 4 shows the monotonic increase in emissivity that occurs for both polarizations as the surface changes from calm water to frazil ice to thin pancakes (approximately 15 cm in diameter) to densely packed pancakes (3 cm thick and about 50 cm in diameter). This monotonic behavior of emissivity can be useful for the retrieval of ice thickness data. An important property of the mi-

crowave signatures is the increase in polarization as ice starts to form on open water. As the ice cover increases polarization rapidly decreases to the first-year ice spectra shown in Fig. 3. On the other hand, when the total backscattering coefficient  $\gamma$  is considered for the transition from open water to thick pancakes, it is found that  $\gamma$  does not show a monotonic variation. At first  $\gamma$  decreases because of the damping of the capillary waves. When the pancakes get larger and thicker  $\gamma$  increases rapidly because of the increase in roughness. When the pancakes exceed a certain size (approximately 0.5 m), the backscattering coefficient decreases again because of the decrease in the density of the edges. At a  $50^\circ$  angle of incidence the maximum backscattering coefficients at 10.4 GHz equal those of multiyear ice, whereas for large pancakes,  $\gamma_{vv} \approx \gamma_{hh} \leq 0.05$  (16), which is less than half that of multiyear ice.

The brightness temperatures at 4.9 and 36 GHz for second-year and multiyear ice floes did not distinguish between the two floe types, even though the freeboard level varied by a factor of 2.5. This indicates that the microwaves emanate from above freeboard level—probably from the snow-ice interface. There the coarse-grained (diameter, 2 to 3 mm) ice crystals produce effective scattering at high microwave frequencies.

#### Aircraft Microwave Observations

The two SAR images in Fig. 5 show how the meteorological regime affects the character of the ice and ocean surface structure. On 19 September the strong easterly winds (10 to 15 m/sec) that had been blowing for several days caused an Ekman drift that compressed the ice edge region and resulted in the generation of a straight, sharp edge (Fig. 5a). Radiation stress from the surface waves may also have contributed to the straight edge. The numerous plumes of ice trailing eastward almost parallel to the edge indicate that the ice pack was moving faster toward the west than the surface water adjacent to the edge. This was verified by comparing the daily mean velocities of ice and water obtained with the drifting ARGOS buoys. Ice velocity in the edge region was nearly 0.3 m/sec to the west and surface water velocity was 0.15 to 0.20 m/sec to the west. The higher ice velocity probably occurred because the wind drag coefficient for ice is greater than that of water (4).

In marked contrast to the SAR image of 19 September (Fig. 5a), the image for 1 October (Fig. 5b) shows the ice to have a wavelike edge with an approximate length scale of 20 to 40 km. Moreover, eddies are present at the ice edge with

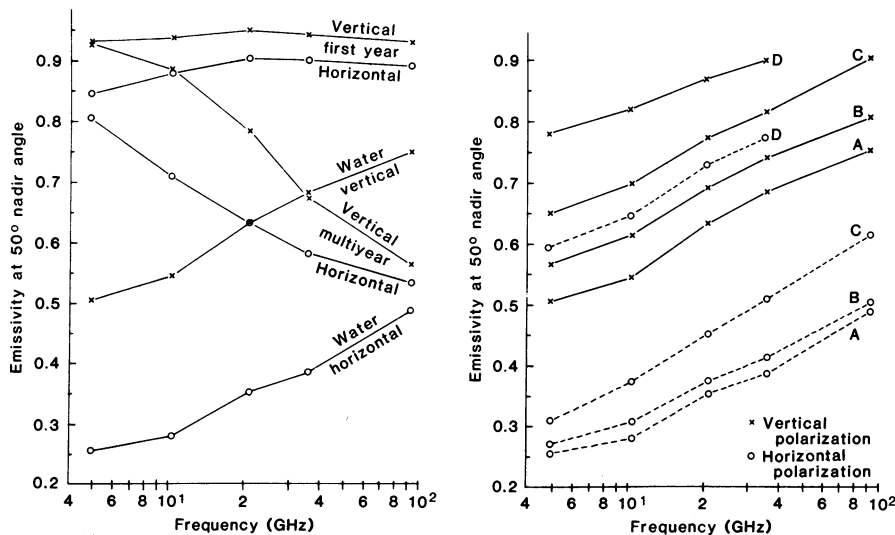


Fig. 3 (left). Measured emissivity of calm water, multiyear ice, and first-year ice as a function of frequency. Fig. 4 (right). Emissivity as the surface changes from calm water (A) to thin frazil ice (B) to thin pancakes covering more than 50 percent of the water (C) to 3-cm-thick, densely packed pancakes (D).

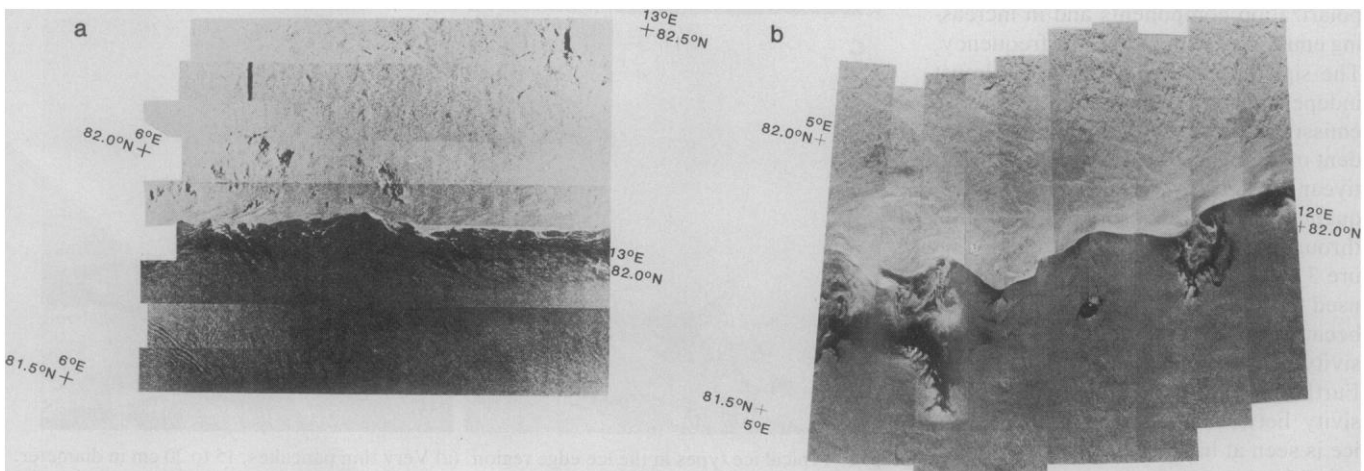


Fig. 5. (a) Image of the marginal ice zone obtained with the SAR (1.215 GHz, horizontal polarization) on 19 September 1979. (b) SAR image of the marginal zone on 1 October 1979.

dimensions of 5 to 15 km. On this day there were light winds, and for the preceding 2 days calm wind conditions had prevailed in the experimental area.

Signatures associated with the eddies ranged from light gray (strong radar backscatter) to almost black (weak backscatter). This is schematically represented in Fig. 6, which also shows the flight and ship tracks. A black, circular signature 5 km across appears in the ocean 20 km off the ice edge, between the two eddies. This black signature also occurs sporadically along the ice edge. These signatures were identified by the microwave instruments on the C-130 and in ice observer reports and ship observations from the tracks shown in Fig. 6.

The low and high SFMR brightness temperatures (Fig. 7a) along track 5 indicate water and ice, respectively. The intermediate brightness temperatures in the eddy regions indicate either lower ice concentrations or very thin ice. The ice observer logged the presence of 100 percent grease ice along tracks 13, 15, and 16 (low-level flights) in positions corresponding to the black signature. The black signature is thus identified as 100 percent grease ice. The low SAR backscatter (6 dB below that of water) (Fig. 7b) from grease ice is associated with the damping of surface waves.

Figure 7b shows the variation in the surface temperature, salinity, and brightness temperature at 4.9 GHz along the track from S1 to S2 and the backscatter profile from the SAR image acquired 6 hours later. The region of low backscatter and high brightness temperature, grease ice, is associated with a 5-km region of water colder and less saline than its surroundings. This is interpreted as an eddy shed from the ice edge. And indeed, the oceanographic section from stations 214 to 222 (Fig. 6), obtained 24 hours before the radar image, indicates an eddy centered at station 219. Another eddy centered at station 216 may be associated with the grease ice region at the ice edge. These eddies are 5 to 15 km in diameter and are up to 150 m deep. The ice bands in the prominent eddies (Fig. 5b) have a cyclonic rotation that suggests a positive vorticity in the ice edge region. This is confirmed by the ice and ocean velocities obtained from the drifting ARGOS buoys for this day. The generation of these eddies is attributed to barotropic instability (4).

A systematic comparison of active and passive microwave signatures for different ice types can be made with a cluster diagram. Figure 8 shows SFMR brightness temperatures plotted against AMS-CAT radar cross sections for beam-filling measurements (from all flights) of

water, nilas (a thin, elastic type of ice formed on a calm sea), gray ice, thick pancakes, and multiyear ice. The good separation of the different ice types enables ice type classification to be made from this combination of active and passive instruments. This technique was suggested earlier by Livingstone *et al.* (17) and has been used for remote sensing of snow (11).

### Comparison of Aircraft and Ship Microwave Observations

The R.V. *Polarsirkel* operated no more than 15 km in from the ice edge, whereas the C-130 flew up to 250 km in from the edge. A comparison of the signatures of corresponding ice types measured from the ship and from the aircraft should indicate the region for

Fig. 6. Schematic representation of the SAR image of 1 October, showing the ice edge, eddies, and grease ice. Thin lines show the flight tracks of the NASA C-130 and the zigzag ship track on 1 October. Black dots indicate the CTD section from stations 214 to 222 obtained on 30 September.

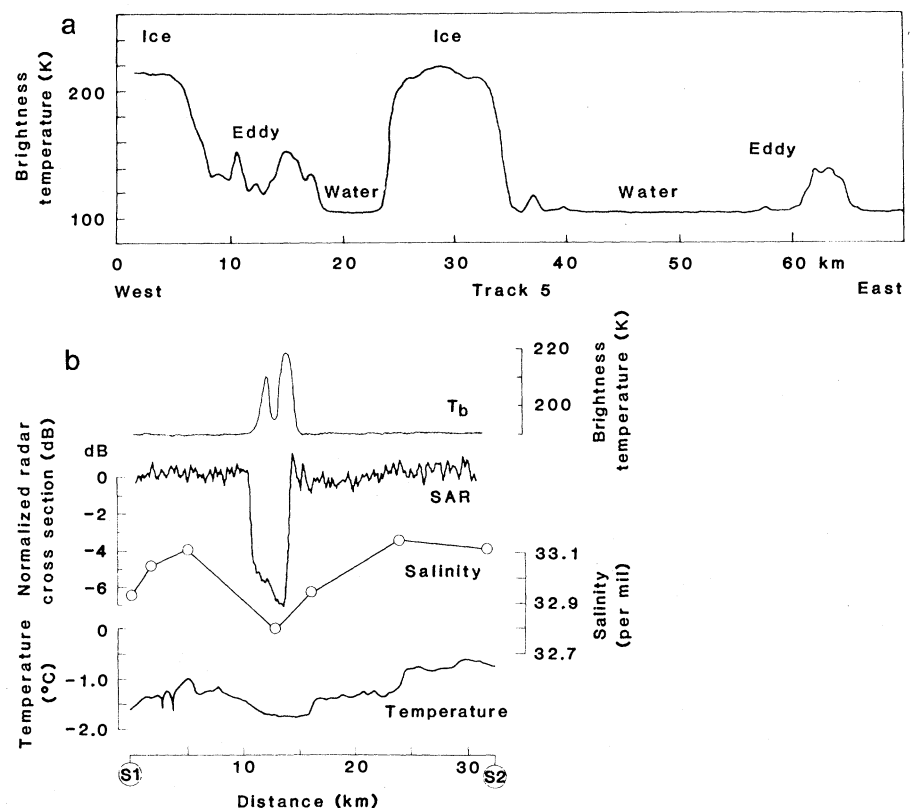
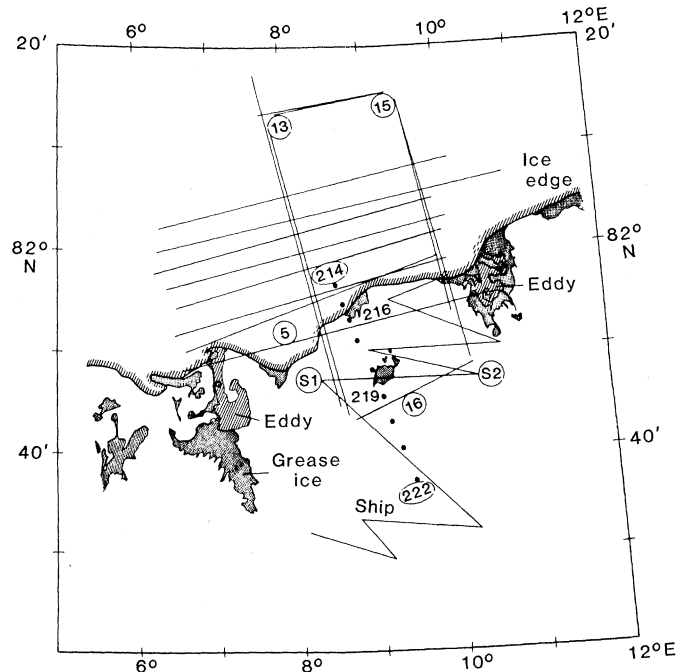


Fig. 7. (a) Brightness temperature measured by the SFMR at 6.6 GHz on 1 October along track 5. (b) Surface temperature and salinity from the R.V. *Polarsirkel*, SAR backscatter (relative scale), and ship-based brightness temperature on 1 October along the track from S1 to S2.

which the ship-based measurements of emissivity are valid.

The difference between the SFMR result and the result from the ship at 6.6 GHz was less than 1 K. The difference between the MFMR and PMIS results and the ship-based measurements was in most cases less than 5 K. This somewhat larger difference is partially explained by the higher accuracy of the SFMR. The ship-based measurements of emissivity can therefore be used with confidence when the snow cover on the ice is dry. These emissivities are being used in algorithms for retrieving geophysical parameters from Nimbus 7 SMMR measurements (3).

### Evaluation of Ice Edge Detection by the Nimbus 7 SMMR

Previous results from the electrically scanning microwave radiometer (ESMR) on Nimbus 5 showed that microwave measurements from space have an all-weather day and night capability of detecting the ice edge (18). However, the

accuracy of the measurements is not known, since no comparison with surface data has been made. Such a comparison was done during NORSEX-79 for the Nimbus 7 SMMR.

The best spatial resolution for locating the ice edge is obtained by using the 37-GHz channels. The horizontally polarized channel is used because it shows a stronger contrast in emissivity between water and multiyear ice (Fig. 3).

Brightness temperatures from the SMMR (37 GHz) for two orbits on 1 October are plotted in Fig. 9 along a line perpendicular to the ice edge, together with the brightness temperature at 6.6 GHz from the C-130 SFMR along the same line. The aircraft navigation is accurate to within 5 km and the Nimbus 7 SMMR positioning is adjusted to within 10 km from the contours of Svalbard on the microwave image. The satellite made measurements about 6 hours earlier than did the aircraft. From the ice edge movement estimated from the ARGOS buoys, the SMMR data were adjusted 3 km north to permit comparison.

Due to the relatively large footprint of the Nimbus 7 SMMR, the ice edge signature is smeared compared to the aircraft measurements. When the ice edge positions from the SMMR are compared with positions obtained from the SAR, the SFMR, the ship, and the buoys (adjusted for distance from the ice edge), the mean differences are 10, 7, 4, and 9 km, respectively. In all cases the SMMR edge is south of the other estimated positions. However, errors due to satellite and aircraft positioning, the time difference between observations, and fluctuations in the distance of the buoys from the edge are estimated to be  $\pm 10$  km. Thus the differences involved are not statistically significant, and one may conclude that the ice edge location obtained with the Nimbus 7 SMMR is accurate to within about 10 km. A large part of this error is due to uncertainty in SMMR pixel locations.

### Conclusions

Microwave signatures from measurements at 5 to 100 GHz are excellent for remote sensing of sea ice. The large contrast in emissivity between water and all ice types at low frequencies facilitates the retrieval of data on total ice concentration. At high frequencies the contrast between first and multiyear ice can be used to separate ice types. A promising alternative for determining ice concentration with improved spatial resolution from satellites is to obtain the polarization information at a frequency of 90 GHz or higher. Consequently, the atmospheric windows at 90 and 140 GHz should be explored for application in future satellites. Moreover, the monotonic increase of emissivity with increasing thickness of new ice can be used to estimate ice thickness up to approximately 5 cm. Comparison with aircraft data indicates that the emissivities measured from the ship are also valid farther into the ice pack. Consequently, they are now being used in algorithms for retrieving geophysical parameters from satellite observations (3). The combination of active and passive microwave measurements also shows promise for ice type identification. The SAR images show a well-defined ice edge under both calm and perturbed wind conditions. During calm conditions, the ice edge reflects the ocean dynamics with a length scale on the order of 10 km, while during strong winds the ice edge reflects atmospheric forcing. Finally, the Nimbus 7 SMMR locates the ice edge accurately to within 10 km.

### References and Notes

1. P. Gloersen *et al.*, *Proceedings of the Cospar/SCOR/IUCRM Symposium of Oceanography from Space*, J. F. R. Gower, Ed. (Plenum, New York, 1981), pp. 717-726.
2. O. M. Johannessen and M. Mork, *Kyststrømrapport 3/79* (Geophysical Institute, Division A, University of Bergen, Bergen, Norway, 1980).
3. E. Svendsen *et al.*, *J. Geophys. Res.* **88**, C5, 2781 (1983).
4. O. M. Johannessen *et al.*, *ibid.*, p. 2755.
5. World Meteorological Organization, *Sea Ice Nomenclature* (Secretariat of the World Meteorological Organization, Geneva, 1970), vols. 1 and 2.
6. T. E. Vinje, *LANDSAT Report E-77-10206* (TID 28540, National Technical Information Service, Springfield, Va., 1977).
7. P. Gloersen and F. T. Barath, *IEEE J. Oceanic Eng.* **OE-2** (No. 2), 172 (1977).
8. W. E. Brown, Jr., C. Elachi, T. W. Thompson, *J. Geophys. Res.* **81**, 2657 (1976).
9. E. Schanda, R. Hofer, D. Wyssen, A. Musy, P. Maylan, C. Morzier, W. Good, paper presented at the Twelfth International Symposium on Remote Sensing of the Environment, Manila, Philippines (1978).
10. R. Hofer and E. Schanda, *Radio Sci.* **13**, 365 (1978).
11. C. Mätzler, E. Schanda, R. Hofer, W. Good, in *Proceedings of the Microwave Remote Sensing of Snowpack Properties Workshop*, A. Rango, Ed. (NASA Conf. Publ. 2153, Greenbelt, Md., 1980), pp. 203-223.
12. A CTD is an instrument that makes continuous measurements of conductivity, temperature, and depth as it is lowered through the water. With these measurements it is possible to calcu-

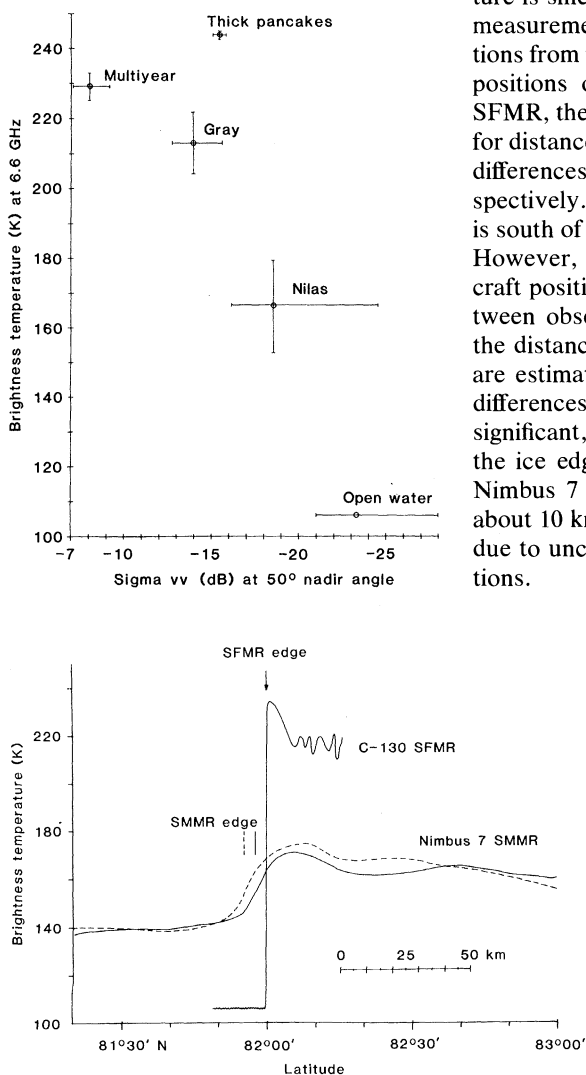


Fig. 8 (top left). Aircraft measurements of brightness temperature (K) at 6.6 GHz plotted against radar cross sections [ $\sigma_{vv}$ (dB)] at 14.6 GHz. Bars indicate variability of the signatures of the selected ice types. Fig. 9 (bottom left). Brightness temperature measured by the SMMR at 37 GHz (horizontal polarization, two orbits) and brightness temperature measured by the SFMR at 6.6 GHz along a line perpendicular to the ice edge.

- late the salinity and density of the water as well as other variables.
13. W. H. Peake, *IEEE Trans. Antennas Propag. AP-7*, 324 (1959).
  14. A. Stogryn, *IEEE Trans. Microwave Theory Tech. MTT-19*, 733 (1971).
  15. J. Fulde, thesis, University of Bern Institute of Applied Physics, Bern, Switzerland (1976).
  16. Like polarization, ( $\gamma_{vv}$ ,  $\gamma_{hh}$ ) refers to a polarization state used for both transmission and reception.
  17. C. E. Livingstone, R. K. Hawkins, A. L. Gray, T. L. Wilkinson, L. D. Arsenault, D. Pearson, K. Okamoto, *Proceedings of the Cospar/SCOR/IUCRM Symposium of Oceanography from Space*, J. F. R. Gower, Ed. (Plenum, New York, 1981), pp. 813–821.
  18. W. J. Campbell, R. O. Ramseier, H. J. Zwally, P. Gloersen, *Boundary-Layer Meteorol.* **18**, 99 (1980).
  19. The NORSEX program was funded by the University of Bergen, Bergen, Norway, the Royal

Norwegian Council for Scientific and Industrial Research (Space Activity Division), the U.S. National Aeronautics and Space Administration (the Jet Propulsion Laboratory contribution was under contract NAS 7100), the U.S. Office of Naval Research (grant 0014-80-G-0003), the U.S. Geological Survey, and the Scientific Affairs Division of the North Atlantic Treaty Organization (grant 9-4-02-SRG.19). The support of the Royal Norwegian Air Force P3 Squadron is gratefully acknowledged.

## Van der Waals Picture of Liquids, Solids, and Phase Transformations

David Chandler, John D. Weeks, Hans C. Andersen

A remarkable revival of the van der Waals picture of liquids occurred during the past two decades. This renaissance was spurred by the discovery (1) from computer simulations that a system of hard spheres (impenetrable “billiard

liquids. But the range of utility of the van der Waals picture is far broader than this limited application might suggest. Its validity and usefulness have been documented in numerous studies extending from computer simulations of condensed

---

*Summary.* The van der Waals picture focuses on the differing roles of the strong short-ranged repulsive intermolecular forces and the longer ranged attractions in determining the structure and dynamics of dense fluids and solids. According to this physical picture, the attractive interactions help fix the volume of the system, but the arrangements and motions of molecules within that volume are determined primarily by the local packing and steric effects produced by the repulsive forces. This very useful approach, its limitations, and its successful application to a wide variety of static and dynamic phenomena in condensed matter systems are reviewed.

---

balls”) has a first-order fluid-solid transition that is intimately related to the freezing and melting transitions of real materials (2). The van der Waals picture stresses the dominant role of the short-ranged harshly repulsive intermolecular forces (which are nearly hard core interactions) in determining the structural arrangements of molecules in a liquid, while neglecting the influence of the longer ranged attractive interactions on the structure. Though originally developed to describe the liquid-gas critical point (3), this approach is now known to be most useful and accurate at the high densities that characterize a liquid away from the critical point, since at those densities the nearly incompressible nature of the fluid tends to inhibit the fluctuations that would invalidate a van der Waals theory.

The successful exploitation of this picture is found in textbook (4) descriptions of perturbation theories of simple atomic

materials, to analytical equilibrium theories of polyatomic organic liquids and mixtures, to models of transport, and even to vibrational relaxation in liquids. In this article we review this powerful perspective and some recent developments.

### The Basic Idea

According to the van der Waals picture, the average relative arrangements and motions of molecules in a liquid (that is, the intermolecular structure and correlations) are determined primarily by the local packing and steric effects produced by the short-ranged repulsive intermolecular forces. Attractive forces, dipole-dipole interactions, and other slowly varying interactions all play a minor role in the structure, and in the simplest approximation their effect can be treated in terms of a mean field—a

spatially uniform background potential—which exerts no intermolecular force and hence has no effect on the structure or dynamics but merely provides the cohesive energy that makes the system stable at a particular density and pressure.

Thus an atom in a monatomic fluid is like a billiard ball and molecules are much like the familiar space-filling models. If one imagines a collection of such objects moving about within a certain volume, colliding elastically with each other and oblivious to any attractive or long-ranged forces between them, then one has a physical picture that captures many essential features of liquid structure and dynamics on a molecular level.

In the modern literature, perhaps the first explicit statements of this picture for monatomic liquids were given by Reiss (5) and by Longuet-Higgins and Widom (2). The idea is much older, however, since it is the primary (though not sole) physical content of the van der Waals equation of state (3). For that reason we attribute the concept to van der Waals, but this historical expedient is not meant to detract from the significance of contributions made by many recent workers to our current understanding of the idea.

The attractive intermolecular interactions rigorously have no effect on the structure only in the hypothetical and unrealistic limit in which the attractive interactions are both infinitely weak and infinitely long-ranged (3, 6, 7). In that case, each particle in the system feels attractive interactions from all the other particles. These interactions exert no net vector force, while the resulting potential energy is accurately described in terms of a spatially uniform mean field. What is significant, however, is that the attractions often continue to have little influence on the structure of real condensed materials, where every atom has several nearest neighbors and packing suppresses large density fluctuations. The spatial variation of real attractions in the intermolecular structures allowed by

---

David Chandler is a professor of chemistry at the University of Illinois, Urbana 61801; John D. Weeks is a member of the technical staff at Bell Laboratories, Murray Hill, New Jersey 07974; and Hans C. Andersen is a professor of chemistry at Stanford University, Stanford, California 94305.